Structural and Electric Properties of Epitaxial Na$_{0.5}$Bi$_{0.5}$TiO$_3$-Based Thin Films

Bruno Magalhaes [1,2,*], Stefan Engelhardt [1,2], Christian Molin [3], Sylvia E. Gebhardt [3], Kornelius Nielsch [1,2] and Ruben Hühne [1]

[1] Leibniz-IFW Dresden, Institute for Metallic Materials, 01069 Dresden, Germany; s.engelhardt@ifw-dresden.de (S.E.); k.nielsch@ifw-dresden.de (K.N.); r.huehne@ifw-dresden.de (R.H.)
[2] Institute of Material Science, Faculty of Mechanical Science and Engineering, TU Dresden, 01062 Dresden, Germany
[3] Fraunhofer IKTS, Fraunhofer Institute for Ceramic Technologies and Systems, Winterbergstraße 28, 01277 Dresden, Germany; christian.molin@ikts.fraunhofer.de (C.M.); sylvia.gebhardt@ikts.fraunhofer.de (S.E.G.)
* Correspondence: b.magalhaes@ifw-dresden.de

Abstract: Substantial efforts are dedicated worldwide to use lead-free materials for environmentally friendly processes in electrocaloric cooling. Whereas investigations on bulk materials showed that Na$_{0.5}$Bi$_{0.5}$TiO$_3$ (NBT)-based compounds might be suitable for such applications, our aim is to clarify the feasibility of epitaxial NBT-based thin films for more detailed investigations on the correlation between the composition, microstructure, and functional properties. Therefore, NBT-based thin films were grown by pulsed laser deposition on different single crystalline substrates using a thin epitaxial La$_{0.5}$Sr$_{0.5}$CoO$_3$ layer as the bottom electrode for subsequent electric measurements. Structural characterization revealed an undisturbed epitaxial growth of NBT on lattice-matching substrates with a columnar microstructure, but high roughness and increasing grain size with larger film thickness. Dielectric measurements indicate a shift of the phase transition to lower temperatures compared to bulk samples as well as a reduced permittivity and increased losses at higher temperatures. Whereas polarization loops taken at −100 °C revealed a distinct ferroelectric behavior, room temperature data showed a significant resistive contribution in these measurements. Leakage current studies confirmed a non-negligible conductivity between the electrodes, thus preventing an indirect characterization of the electrocaloric properties of these films.

Keywords: ferroelectrics; epitaxy; thin films; pulsed laser deposition

1. Introduction

Materials with distinct ferroelectric properties enable the direct conversion between thermal, mechanical, and electrical energies, which are utilized in devices such as actuators, transducers or sensors [1–3]. More recently, the conversion of electrical to thermal energy by using the so-called electrocaloric effect (ECE) received renewed interest due to its potential for realizing energy-efficient solid-state cooling devices [4,5]. Starting with the work of Mischenko et al. on PbZr$_{0.95}$Ti$_{0.05}$O$_3$ [6], giant electrocaloric effects were measured in thin films. Whereas a number of other lead-containing materials show large temperature changes due to the ECE [5], the major focus of the present research has moved towards environmentally friendly, lead-free materials. The majority of research was performed on BaTiO$_3$-based thin films due to their well-established preparation routes as well as the tunable structural and ferroelectric properties [7–13]. In the quest for alternative materials, Na$_{0.5}$Bi$_{0.5}$TiO$_3$ (NBT)-based compounds were also tested for their ECE, and significant temperature changes of up to 1.5 K (at 50 kV cm^{-1} and 135 °C) were found for bulk NBT-based compound [14,15]. Due to the breakdown voltage limitation (∼50 kV cm^{-1}) [6,16] of bulk materials, the change in temperature might be significantly higher in thin films, as

larger electric fields can be applied, leading to a higher ΔT, especially close to a ferroelectric phase transition [4,17,18]. At the same time, this material system might be used for basic studies on the correlation between structure, composition, ferroelectricity, and electrocaloric properties, which is simplified in epitaxially grown layer architectures. Therefore, it was our goal to realize such epitaxial thin films of NBT-based materials to enable these detailed studies in the next step.

As first reported by Smolenskii et al. [19], NBT is a pseudo-cubic perovskite oxide with a rhombohedral phase at room temperature [20], which exhibits two subsequent phase transitions (rhombohedral-tetragonal and tetragonal-cubic) with increasing temperature [21–23]. Different deposition techniques, such as sputtering [24,25], chemical sol-gel processes [26,27], and pulsed laser deposition (PLD) [28–30], have been used so far to realize NBT thin films. It was found in these studies that the target stoichiometry and the PLD deposition conditions have a strong influence on the NBT growth and the final properties [21,28,31]. Hence, using optimized growth parameters is an essential requirement for high-quality films. Simultaneously, the phase transition temperature can be tuned by modifying the composition of the films, which might be beneficial for applications as the ECE is significantly enhanced in the vicinity of the phase transitions. In the case of NBT, the phase transition temperatures can be modified by doping with other oxides as $BaTiO_3$ or $SrTiO_3$ [32–34]. As one example, Hiruma, Y. et al. [32,33] showed that the phase transition temperature decreases with increasing $SrTiO_3$ content, even reaching a critical point where NBT transforms directly from the rhombohedral to the cubic phase. The doping of NBT with $BaTiO_3$ as well as with $SrTiO_3$ results in improved electrocaloric properties with temperature changes of up to 1.64 K at 50 kV cm^{-1} [35,36]. A double doping of NBT by Sr and Ba was studied by Tang et al. [37], indicating that the temperature of a maximum ECE might be further optimized, resulting additionally in wider cooling peaks.

As already mentioned above, the aim of our recent work is to study the structural and ferroelectric properties of epitaxially grown NBT thin films with the emphasis to realize suitable layer architectures for future detailed electrocaloric studies. The importance of optimized deposition conditions for the epitaxial growth of NBT-based thin films on single crystalline substrates was already mentioned. Therefore, we will show how the misfit to the substrate as well as the deposition temperature during PLD affects the orientation and the microstructure of NBT-based thin films. Such optimization of the deposition parameters was essential to obtain an epitaxial growth. However, polarization and leakage current measurements indicate a significant resistive contribution even for optimized films, which does not allow for the characterization of the ECE.

2. Materials and Methods

The growth of $Na_{0.5}Bi_{0.5}TiO_3$-based thin films was performed on buffered $SrTiO_3$ (STO), $YAlO_3$ (YAO), and $LaAlO_3$ (LAO) single crystals having a (001) (pseudo)cubic surface structure using pulsed laser deposition. Prior to deposition, the substrates were ultrasonically cleaned in an acetone bath, cleansed with isopropanol, and blow-dried with argon. The substrates were attached to a heater in a high vacuum chamber with a base pressure of about 10^{-6} mbar. Afterwards, the films were grown using a KrF (248 nm) excimer laser (Coherent LaserSystem, Göttingen, Germany) in a standard on-axis geometry, where the target and substrate were parallel to each other. The distance between the target and substrate was set to 5 cm. A sintered $La_{0.5}Sr_{0.5}CoO_3$ (LSCO) target was used to deposit an epitaxial buffer layer on the substrates with a thickness of about 20 nm, acting later as a bottom electrode. All LSCO layers were deposited with a substrate temperature T_S of 550 °C, a laser fluence w of 1.5 J cm^{-2}, a frequency f of 10 Hz, and an oxygen background pressure p_{O_2} of 0.3 mbar. Pure NBT as well as $Na_{0.38}Bi_{0.38}Sr_{0.19}Ba_{0.06}TiO_3$ (NBSBT) thin films were deposited at temperatures T_S between 550 °C and 650 °C using similar deposition parameters as for the LSCO buffer. The number of laser pulses was adjusted to attain the intended film thickness. The stoichiometric targets were prepared from Na_2CO_3, Bi_2O_3, TiO_2, $BaCO_3$, and $SrCO_3$ powders by a solid-state reaction route with

several grinding and sintering steps [38]. X-ray diffraction (XRD) measurements confirm the phase purity of the NBT target, whereas still separated peaks for the BNT and the STO phase were found in the NBSBT target (compare Supplementary Materials Figure S1).

X-ray diffraction measurements were performed on the grown films in a standard θ-2θ goniometer using Co-K$_\alpha$ radiation (D8 Advance, Bruker AXS, Karlsruhe, Germany) to study the phase composition and crystal structure. The film orientation was analyzed by texture measurements carried out on a four-circle diffractometer (Philips X'pert PW 3040, Panalytical, Almelo, Netherlands) using Cu-K$_\alpha$ radiation, whereas in-plane and out-of-plane lattice parameters were determined by using reciprocal space mapping (RSM) in a similar device. The surface morphology was studied by atomic force microscopy (AFM) using a Bruker Dimension Icon Scanning Probe Microscope (Bruker Nano Surfaces, Karlsruhe, Germany) in tapping mode. The microstructure of selected films was characterized by scanning electron microscopy (SEM) of cross-sections prepared with a focused ion beam (FIB) technique in a dual beam FEI Helios 600i device (FEI Company, Hillsboro, OR, USA).

Dielectric measurements were performed using LSCO as the bottom electrode and platinum as the top electrode. The deposition of Pt top electrodes with an approximate diameter of 200 μm was realized by a conventional sputtering process at room temperature. The polarization p (measured with a frequency of 1 kHz) and the leakage current were characterized in a temperature range from -100 °C to room temperature using a Radiant Technologies Precision Multiferroic tester (Radiant Technologies, Albuquerque, NM, USA). The dielectric properties were measured with an impedance analyzer HP 4284A Precision LCR meter (Hewlett Packard, Palo Alto, CA, USA) connected to a Linkam temperature stage. Capacitance C and the dissipation factor tan δ of the prepared films were determined with an oscillating stimulus of 50 mV. The frequency and temperature-dependent dielectric permittivity ε_r were determined from these data using the relation $C = \varepsilon_0 \varepsilon_r A/d$ with a film thickness d, an area of Pt electrode A, and vacuum permittivity ε_0. These measurements were performed upon cooling from 350 °C to -150 °C.

3. Results

The study of dielectric and ferroelectric properties of epitaxial NBT-based films as well as the subsequent characterization of the ECE by the indirect method requires dense layers with smooth interfaces. In the following, we will summarize our efforts to realize such epitaxial NBT film architectures on different substrates using optimized deposition temperatures. Afterwards, we will discuss the growth of NBT layers doped simultaneously with BaTiO$_3$ and SrTiO$_3$. Here, we choose a composition, which revealed a good electrocaloric properties close to room temperature as bulk material [37].

3.1. Undoped Na$_{0.5}$Bi$_{0.5}$TiO$_3$ Films
3.1.1. Structural Characterization

Based on literature data [21,28], the deposition parameters were tuned to find optimized conditions for epitaxial growth of the NBT-based thin films. As the first step, different single crystalline substrates were tested. Therefore, pure NBT films were deposited on LSCO-buffered LAO ((pseudo)cubic lattice parameter a = 3.79 Å), YAO (a = 3.71 Å), and STO (a = 3.905 Å) substrates at temperatures between 550 °C and 650 °C. The XRD patterns show mainly (00ℓ) peaks of NBT film, which are close to the related (00ℓ) substrate peaks (compare Figure 1a) for LAO and YAO). It should be mentioned that the NBT peaks are barely visible for the films on the STO substrates due to similar c-axis lattice parameters (3.89 Å and 3.905 Å for NBT and STO, respectively, compare Figure S2); therefore, detailed studies were mainly continued with the other two substrates. In the case of the NBT layer deposited on YAO, an additional small peak for a (110) crystal orientation is visible at a 2θ angle of about 37.9° for the samples deposited at 550 °C and 650 °C. In all XRD patterns, reflections emerging from the LSCO buffer layer are hardly visible due to the low film thickness of about 20 nm and the partial overlapping with the strong substrate peaks. The

out-of-plane lattice parameters of 3.97 Å $\pm$ 0.03 Å for the samples deposited on LAO and YAO substrates are significantly larger than the target material (a = 3.88 Å), but in the same range as the values of other groups [39], indicating already a tetragonal distortion of the unit cell.
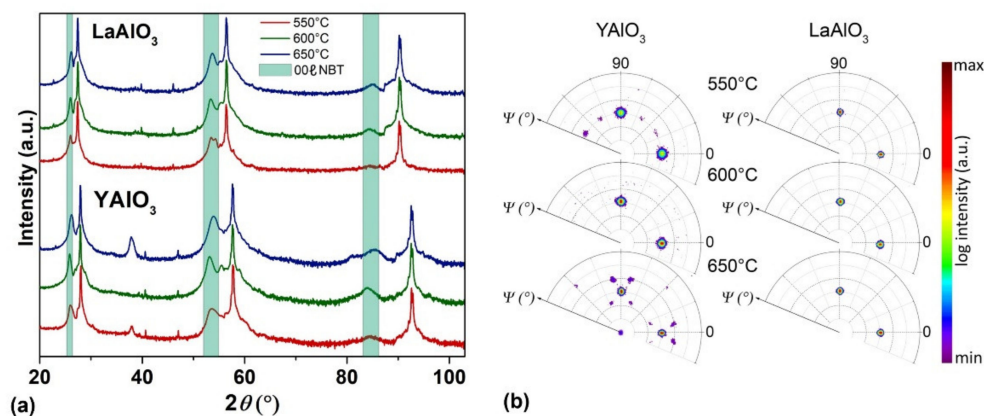

Figure 1. (**a**) XRD scans showing the influence of the substrate and the deposition temperature on the growth of NBT films with a thickness of about 150 nm; (**b**) Pole figure measurements of the (110) NBT peak for films grown on YAO and LAO substrates at different deposition temperatures.

Pole figure measurements were used to study the epitaxial relationship between the NBT layer and the single crystal substrates as a function of temperature (Figure 1b). All (110) pole figures show mainly a four-fold symmetry indicating an epitaxial transfer of the orientation from single crystal through the LSCO buffer layer to the NBT thin film. However, the pole figures of NBT grown on YAO at 550 °C and 650 °C show minor additional reflections arising from different texture components, whereas an undisturbed epitaxial growth is observed at 600 °C. In contrast, no other texture components are found for the films grown on LAO substrates for the studied temperature range, resulting in an epitaxial relationship of NBT(001)[100]||LSCO(001)[100]||LAO(001)[100] (using the pseudo-cubic notation for the rhombohedral single crystal). The origin of such a substrate dependence might be found in differences of the lattice parameters for the used single crystals.

Detailed RSM measurements indicate a relaxed growth of the LSCO buffer layer on YAO due to a lattice misfit of about 3.6% (see Figure 2a), whereas this layer is strained on LAO due to a smaller misfit of about 1.3% (compare Figure 2b). As a result, more defects can be assumed at the LSCO surface grown on YAO in comparison to LAO, which is additionally supported by the broadening of the buffer layer peak in reciprocal space. This might influence the nucleation of the subsequent NBT layer, resulting in a larger temperature window for undisturbed epitaxial growth on LAO. As a consequence, films deposited at a temperature of 550 °C on LAO were preferentially used for further studies on the epitaxial growth of NBT-based materials. The NBT in-plane lattice constant was determined to 3.85 Å for LAO, giving a tetragonal distortion of 1.3%, whereas a value of 3.89 Å was found on YAO. However, the diffraction spots of the NBT (103) peak are significantly broadened in the RSM maps, which might be the result of small sizes of coherent scattering (i.e., a small grain size and/or a large number of defects) as well as strain and compositional gradients.

Finally, the influence of the substrate on the surface morphology was studied. AFM scans were performed for films with similar thickness grown on different substrates. The film on YAO shows a heterogeneous structure with a small grain size and a high number of protruding, almost quadratic grains having a size of about 50 nm (Figure 3a). A root mean square (rms) roughness of 5.4 nm was determined for this image. A slightly smaller roughness was found for the sample on the LAO substrate (Figure 3b) with an rms value of 4.3 nm. Again, protruding grains with a height of up to 50 nm are found on the surface. The

rough surface was confirmed in FIB cross section as shown for one example in Figure 3c. The high roughness with the protruding gains might impede the measurement of dielectric and ferroelectric properties; nevertheless, a basic electric characterization was performed.
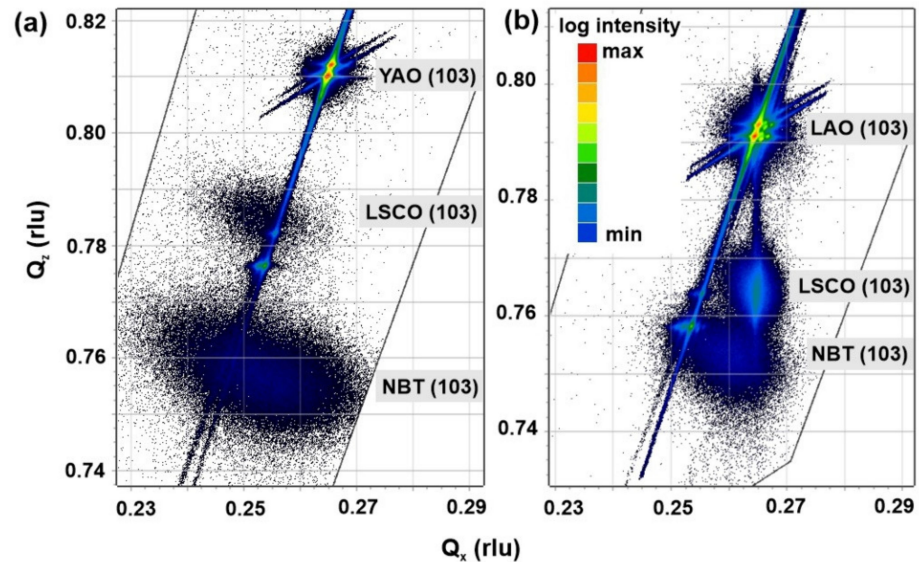

Figure 2. RSM maps for NBT films grown on: (**a**) YAO (T_s = 600 °C) and (**b**) LAO (T_s = 550 °C) substrates using a LSCO buffer layer.
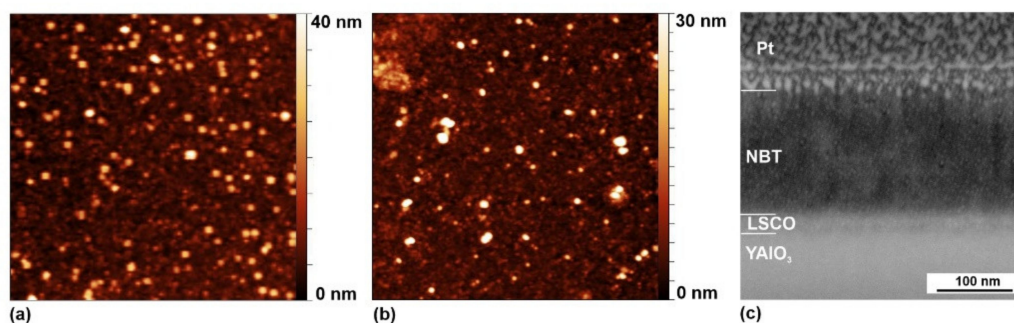
Figure 3. AFM images with a size of 5 μm by 5 μm of about 150-nm-thick NBT layers grown at 550 °C on (**a**) YAO and (**b**) LAO; (**c**) FIB cross section of the NBT layer grown on YAO/LSCO substrate.

3.1.2. Polarization and Leakage Current Characterization

After the preparation of Pt contacts, polarization hysteresis loops $P(E)$ and leakage currents were measured for selected samples at room temperature for an applied electric field of up to 500 kV cm^{-1}. Exemplary results are shown in Figure 4a,b for an NBT layer grown on a LSCO/LAO substrate at 550 °C. It is apparent that the polarization loop shows no clear sign of ferroelectric behavior due to its almost oval shape. Such curves typically arise from the resistive behavior of the layer, i.e., conducting paths between the electrodes [40,41]. To verify this, leakage current measurements were performed, which are shown in Figure 4b. The results indicate an exponential increase in the current density with applied electric field for both polarities. For the positive branch, a maximum of 1.7×10^{-4} A cm^{-2} was found for a field of 500 kV cm^{-1}, while an increase in the leakage current to even 2.4×10^{-2} A cm^{-2} is measured for the negative branch. Films deposited at higher temperature or on the YAO substrate exhibit a similar behavior with even higher resistive contributions. The high surface roughness with the protruding grains, additional pores (not shown), and a high number of defects, such as, oxygen vacancies, might be

responsible for such high leakage currents, which also prohibited the measurement of temperature-dependent dielectric properties.
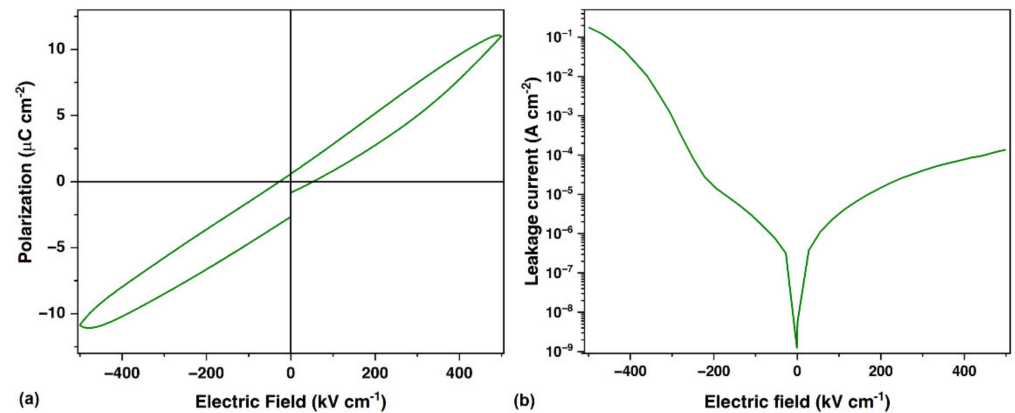

Figure 4. (**a**) *P(E)* measurement at room temperature with a frequency of 1 kHz and (**b**) leakage current measurement at room temperature for an NBT layer grown on a LAO/LSCO substrate (T_s = 550 °C).

In summary, an epitaxial growth of pure NBT layers was realized with the largest parameter window for LAO substrates. However, high roughness and high leakage currents were found for all samples, which prohibits the dielectric characterization and results in poor ferroelectric properties. Therefore, we focused in the following on doped NBT films in order to study if the additional $BaTiO_3$ and $SrTiO_3$ content resulted in improved thin film properties for this material.

3.2. Epitaxial $Na_{0.38}Bi_{0.38}Sr_{0.18}Ba_{0.06}TiO_3$ Films on $LaAlO_3$

3.2.1. Structural Characterization

Based on the results for pure NBT films, epitaxial $Na_{0.38}Bi_{0.38}Sr_{0.18}Ba_{0.06}TiO_3$ (NBSBT) layers were grown on LSCO-buffered LAO substrates at different deposition temperatures. The XRD patterns show mainly (00ℓ) peaks of the NBSBT film which are close to the related substrate peaks (Figure 5a).
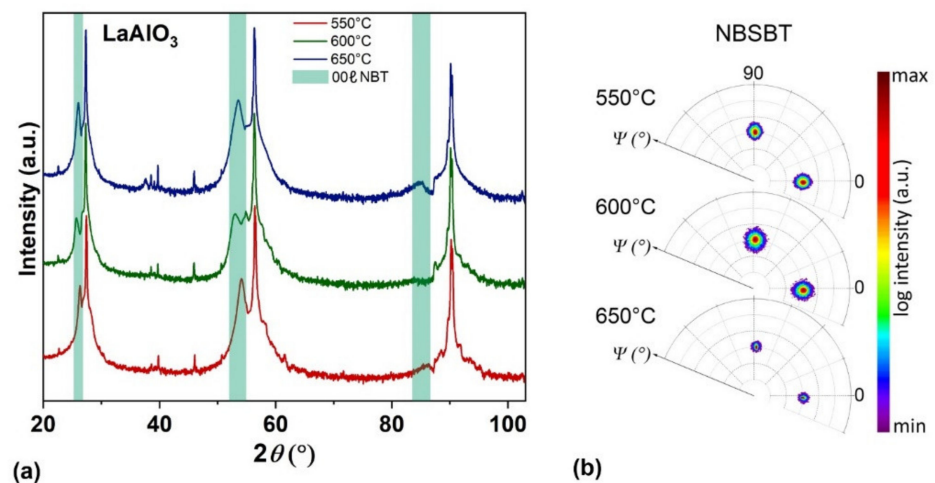

Figure 5. (**a**) XRD scans of NBSBT grown on LAO substrates at different temperatures; (**b**) Pole figure measurements of the (110) NBSBT peak for NBSBT films grown on LAO substrates at different deposition temperatures.

In contrast to the measurement of the target, no separated peaks for the NBT and the STO phase were found, indicating an incorporation of Sr (and Ba) in the NBT crystal structure during the PLD process. The similar lattice parameters of LSCO and the LAO substrate lead again to a partial overlapping of buffer layer reflections with the strong substrate peak, which are therefore barely visible. The out-of-plane lattice parameters are 3.95 Å $\pm$ 0.03 Å slightly smaller compared to the pure NBT films. Pole figure measurements were used to study the epitaxial relationship between the NBSBT layer and the single crystalline substrate (Figure 5b). As for pure NBT, all (110) pole figures show a four-fold symmetry, indicating an epitaxial transfer of the orientation from the LAO single crystal through the LSCO buffer layer to the NBSBT thin film. No other texture component is found for this material for all studied deposition temperatures.

Additionally, the influence of the film thickness was studied on NBSBT layers. Figure 6a shows the XRD scans close to the (001) substrate peak for three different films. The two thinner films were deposited with a deposition rate of about 0.15 nm/s using the same condition as for all other NBT films discussed above. In contrast, the NBSBT film with a thickness of about 1 µm was grown significantly faster with a rate of about 1 nm/s. The films with 75 nm and 250 nm thickness show (00ℓ) peaks with a slight shift of the lattice parameter towards larger values (i.e., smaller 2θ values). Similar results were also found for other thicknesses up to 400 nm using the same deposition rate (scans not shown). In contrast, the 1-µm-thick film shows an even larger out-of-plane lattice cell as well as an additional (110) peak.
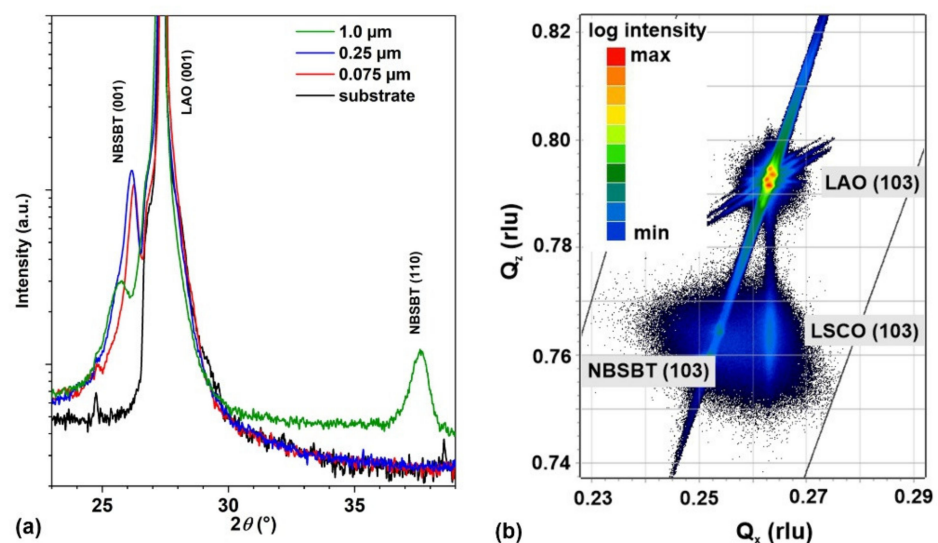

Figure 6. (**a**) XRD-scans of NBSBT films with different thicknesses grown on LSCO-buffered LAO substrates.; (**b**) RSM map of the (103) peaks for a 400-nm-thick NBSBT layer grown on LSCO buffered LAO at $T_s = 550\,^\circ\text{C}$.

The lattice parameters of NBSBT were determined again by RSM; one example is shown in Figure 6b. Similar measurements were performed for the samples deposited at higher temperatures. A strained growth of the LSCO layer was verified for all deposition temperatures by observing similar Q_x-values as for the single crystal peak. The in-plane lattice constants of the NBSBT layer are slightly larger than the substrate with values of about 3.85 Å. The difference between the in-plane and out-of-plane lattice parameters proves again a tetragonal distortion of the unit cell, as found for the pure NBT films.

Cross-sectional SEM images of NBSBT films were used to measure their thickness and to obtain some information about their overall morphology. All samples show a dense structure with columnar grains and some additional pores spreading over the complete film thickness (compare Figure 7a for the 1 µm thick sample). Such columnar structures are typically observed in thin films and might arise from strong island nucleation and

growth. AFM scans were performed for films with different thicknesses to study the surface morphology. The film with a thickness of about 75 nm shows a homogeneous and fine structure with a grain size of about (25 ± 10) nm (Figure 7b). With increasing film thickness, larger grains are observed as shown in Figure 7c,d having an average size of about (45 ± 15) nm for a thickness of 400 nm and 1 µm, respectively. Additionally, agglomerates of the smaller grains having a size of up to 200 nm and larger pores are visible for the thickest film. Simultaneously, the rms roughness increases from 2.6 nm over 5.8 nm to 6.5 nm for the samples shown. The increasing grain size and roughness indicate a coarsening of grains with thickness, where some grains might be overgrown by other grains.
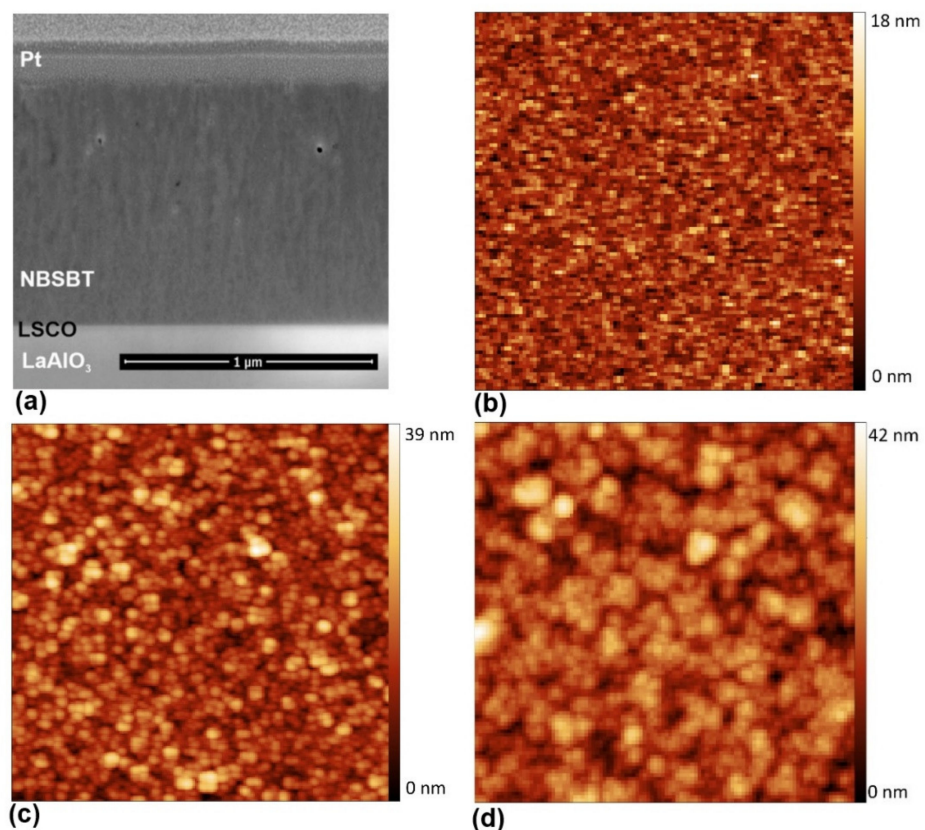

Figure 7. (**a**) Cross-section SEM image of the NBSBT sample with 1 µm thickness; AFM scan with a size of 2×2 µm^2 for NBSBT samples grown at 550 °C with a thickness of: (**b**) 75 nm, (**c**) 400 nm, and (**d**) 1 µm.

3.2.2. Electric Characterization

Temperature-dependent dielectric measurements were performed for all samples in order to evaluate the permittivity. Unfortunately, most of the samples showed again significant leakage currents at higher temperatures, which hindered a detailed analysis. Nevertheless, it was possible to obtain some results for the 1-µm-thick film to compare it with data obtained on bulk material, which was processed similar as the target [38]. Both datasets are shown in Figure 8.

The permittivity of the bulk material shows a dependence on the measuring frequency for temperatures below 130 °C. The tan δ reveals a frequency dependence with a local maximum, which moves to room temperature for lower frequencies. This tan δ peak is considered the depolarization temperature T_d in some studies [32,36]. In contrast, the temperature of maximum permittivity T_m at about 220 °C reveals no frequency dependence while tan δ reaches a minimum. Similar results were obtained by other groups [26]. Figure 8b shows the temperature dependence of the predominately epitaxial film sample

with a thickness of 1 µm. In general, the values for the permittivity are substantially reduced, which is often observed for thin films. At low temperatures, tan δ shows a similar frequency dependent peak as for the bulk material. However, the values are significantly higher, and the maximum is shifted to lower temperatures having a larger shift with frequency. This behavior might indicate a shift of T_d to lower temperatures either due to the tetragonal distortion or stoichiometric changes. For higher temperatures, an increase in tan δ is observed, which might be related to a high leakage current (see below). Due to this fact, the permittivity at high temperatures shows an abnormal increase (not shown in Figure 8b), where no conclusion can be made. Similar to bulk samples, the permittivity presents a low frequency dependence for temperatures between 50 and 200 °C although within a smaller temperature range. Even if the qualitative temperature and frequency dependence of the dielectric properties look similar for bulk and thin film samples, the film data need to be taken with caution as a large resistive contribution was found in leakage measurements as will be discussed in the following.
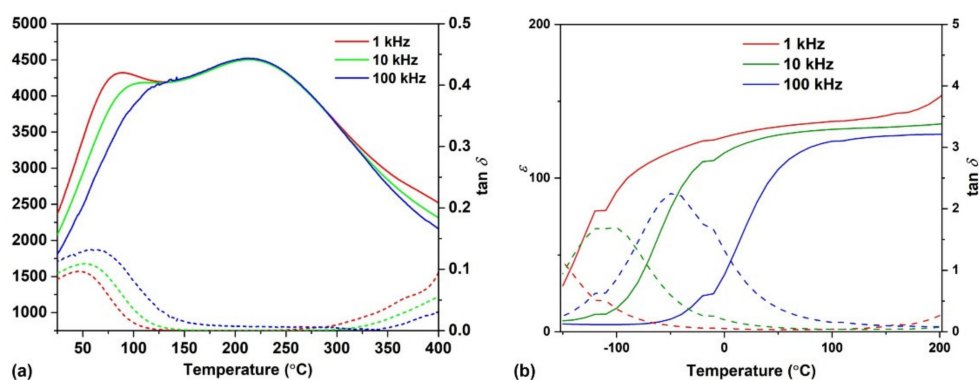

Figure 8. (**a**) Relative permittivity and loss tan δ of bulk NBSBT at different frequencies (data taken from: [38]; (**b**) Relative permittivity and loss tan δ of the 1 µm NBSBT sample grown on LAO.

The influence of temperature on the electric field dependent polarization hysteresis $P(E)$ and on the leakage current is shown in Figure 9a,b for the sample with a thickness of 1 µm. The polarization and leakage current measurements were performed at −100 °C and room temperature with a frequency of 1 kHz. The sample shows a characteristic s-shape and closed polarization loop at low temperatures, which is typical for thin-film material [42]. A maximum polarization of 8.3 µC cm^{-2}, a remnant polarization of 1.2 µC cm^{-2}, and a coercive field of 58 kV cm^{-1} was reached. Whereas the polarization measurements at low temperature indicate symmetric hysteresis loops, results measured at room temperature show an asymmetric behavior. The origin of the different shapes might be mainly due to resistive contributions, i.e., conductive paths through the film resulting in a deformation of the loops [41]. As a result, it is not possible to use these data for the indirect characterization of the ECE due to the need for polarization measurements as a function of the applied temperature over a larger temperature range.

Finally, leakage current measurements were performed to verify the influence of resistive contributions on the observed polarization loops. Currents in the order of about 10^{-6} A cm^{-2} were measured for temperature of −100 °C. However, the values increased significantly if the sample is measured at room temperature. This is consistent with an increasing resistive contribution observed in the temperature-dependent polarization loops. Similar results with slightly higher values were also found for thinner NBSBT films, i.e., the leakage currents tend to decrease with increasing thickness. The observed behavior might be explained by a high density of defects in the samples creating conducting paths between the two electrodes. In particular, the high surface roughness as well as the porosity observed at the surface and in the cross-sections may contribute to this resistive behavior. There might be an additional influence of the columnar grain boundaries. The results of

our measurements are comparable with the literature [31] although measured at lower temperatures but with higher electric fields.
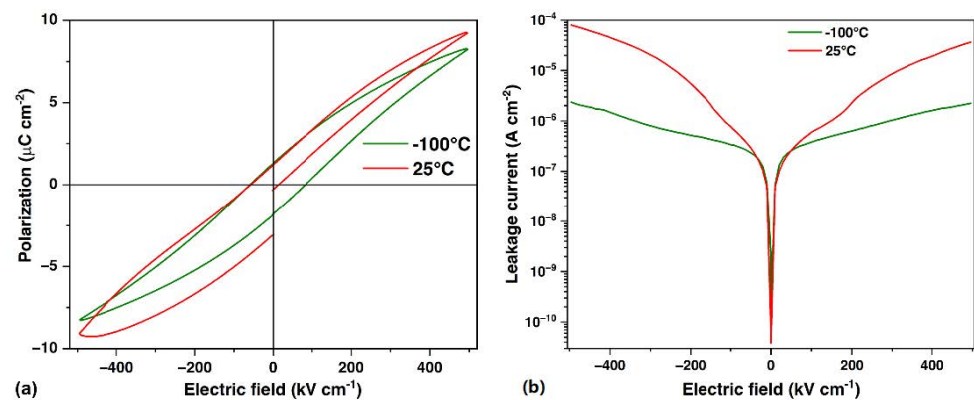

Figure 9. (**a**) $P(E)$ measurements at $-100\,^{\circ}$C and at room temperature for the NBSBT film with 1 μm thickness; (**b**) leakage current measurement at $-100\,^{\circ}$C and room temperature for the same sample.

4. Conclusions

Epitaxial NBT-based thin films were epitaxially grown on LSCO-buffered YAO and LAO substrates by optimizing the deposition parameters. The occurrence of additional texture components in films on YAO indicates only a narrow temperature range for epitaxial growth of NBT on these crystals. In contrast, LAO substrates seem to be more suitable as only a single epitaxial texture component was found in the studied temperature range. Detailed RSM measurements showed a strained LSCO and a relaxed NBT layer having a (0 0 1) orientation and an additional tetragonal distortion. However, a significant roughness with protruding grains was observed even for thin films. Polarization hysteresis and leakage current measurements showed a low film resistivity, which prohibited further ferroelectric and dielectric studies. Similar structural properties were also found for the NBSBT films grown on LAO. Cross-sectional images revealed the presence of a columnar structure throughout the film thickness, whereas a higher surface roughness and an increased grain size were found with increasing thickness. Electric field-dependent polarization loops were measured at $-100\,^{\circ}$C showing a ferroelectric behavior with a maximum polarization up to 8.3 μC cm^{-2} at 500 kV cm^{-1}. However, room temperature measurements revealed a significant resistive contribution in the polarization loops, which hindered the evaluation of the ECE. In summary, whereas an epitaxial growth of NBT-based thin films was demonstrated, a further optimization of the film microstructure is required to reduce the roughness as well as the leakage currents at elevated temperatures. An additional doping with Mn or changes in the stoichiometry might help to improve these properties as discussed by other groups [30,43].

Author Contributions: Conceptualization, R.H.; investigation, B.M., S.E., C.M., and R.H.; resources, C.M., S.E.G., and R.H.; writing—original draft preparation, B.M.; writing—review and editing, R.H.; supervision, S.E.G., K.N., and. R.H.; project administration, R.H.; funding acquisition, R.H. All authors have read and agreed to the published version of the manuscript.

Institutional Review Board Statement: Not applicable.

Informed Consent Statement: Not applicable.

References

1. Scott, J.F. Applications of modern ferroelectrics. *Science* **2007**, *315*, 954–959. [CrossRef] [PubMed]
2. Park, S.-E.; Shrout, T.R. Ultrahigh strain and piezoelectric behavior in relaxor based ferroelectric single crystals. *J. Appl. Phys.* **1997**, *82*, 1804–1811. [CrossRef]
3. Liu, Z.K.; Li, X.; Zhang, Q.M. Maximizing the number of coexisting phases near invariant critical points for giant electrocaloric and electromechanical responses in ferroelectrics. *Appl. Phys. Lett.* **2012**, *101*, 082904. [CrossRef]
4. Fähler, S.; Rößler, U.K.; Kastner, O.; Eckert, J.; Eggeler, G.; Emmerich, H.; Entel, P.; Muller, S.; Quandt, E.; Albe, K. Caloric effects in ferroic materials: New concepts for cooling. *Adv. Eng. Mater.* **2012**, *14*, 10. [CrossRef]
5. Valant, M. Electrocaloric materials for future solid-state refrigeration technologies. *Prog. Mater. Sci.* **2012**, *57*, 980–1009. [CrossRef]
6. Mischenko, A.S.; Zhang, Q.; Scott, J.F.; Whatmore, R.W.; Mathur, N.D. Giant electrocaloric effect in thin-film $PbZr_{0.95}Ti_{0.05}O_3$. *Science* **2006**, *311*, 1270–1271. [CrossRef] [PubMed]
7. Engelhardt, S.; Mietschke, M.; Molin, C.; Gebhardt, S.; Fähler, S.; Nielsch, K.; Hühne, R. Structural and ferroelectric properties of epitaxial $BaZr_xTi_{1-x}O_3$ thin films. *J. Phys. D Appl. Phys.* **2016**, *49*, 495303. [CrossRef]
8. Engelhardt, S.; Molin, C.; Gebhardt, S.; Fähler, S.; Nielsch, K.; Hühne, R. $BaZr_xTi_{1-x}O_3$ epitaxial thin films for electrocaloric investigations. *Energy Technol.* **2018**, *6*, 1526–1534. [CrossRef]
9. Bai, Y.; Ding, K.; Zheng, G.-P.; Shi, S.-Q.; Qiao, L. Entropy-change measurement of electrocaloric effect of $BaTiO_3$ single crystal. *Phys. Status Solidi A* **2012**, *209*, 941–944. [CrossRef]
10. Marathe, M.; Ederer, C. Electrocaloric effect in $BaTiO_3$: A first-principles-based study on the effect of misfit strain. *Appl. Phys. Lett.* **2014**, *104*, 212902. [CrossRef]
11. Marathe, M.; Renggli, D.; Sanlialp, M.; Karabasov, M.O.; Shvartsman, V.V.; Lupascu, D.C.; Grünebohm, A.; Ederer, C. Electrocaloric effect in $BaTiO_3$ at all three ferroelectric transitions: Anisotropy and inverse caloric effects. *Phys. Rev. B* **2017**, *96*, 014102. [CrossRef]
12. Moya, X.; Stern-Taulats, E.; Crossley, S.; González-Alonso, D.; Kar-Narayan, S.; Planes, A.; Mañosa, L.; Mathur, N.D. Giant electrocaloric strength in single-crystal $BaTiO_3$. *Adv. Mater.* **2013**, *25*, 1360–1365. [CrossRef] [PubMed]
13. Zhang, X.; Wang, J.B.; Li, B.; Zhong, X.L.; Lou, X.J.; Zhou, Y.C. Sizable electrocaloric effect in a wide temperature range tuned by tensile misfit strain in BaTiO3 thin films. *J. Appl. Phys.* **2011**, *109*, 126102. [CrossRef]
14. Le Goupil, F.; Alford, N.M. Upper limit of the electrocaloric peak in lead-free ferroelectric relaxor ceramics. *APL Mater.* **2016**, *4*, 064104. [CrossRef]
15. Le Goupil, F.; Bennett, J.; Axelsson, A.-K.; Valant, M.; Berenov, A.; Bell, A.J.; Comyn, T.P.; Alford, N.M. Electrocaloric enhancement near the morphotropic phase boundary in lead-free NBT-KBT ceramics. *Appl. Phys. Lett.* **2015**, *107*, 172903. [CrossRef]
16. Scott, J.F. Ferroelectric memories. *Phys. World* **1995**, *8*, 46–52. [CrossRef]
17. Liu, Y.; Scott, J.F.; Dkhil, B. Direct and indirect measurements on electrocaloric effect: Recent developments and perspectives. *Appl. Phys. Rev.* **2016**, *3*, 031102. [CrossRef]
18. Saranya, D.; Chaudhuri, A.R.; Parui, J.; Krupanidhi, S.B. Electrocaloric effect of PMN-PT thin films near morphotropic phase boundary. *Bull. Mater. Sci.* **2009**, *32*, 259–262. [CrossRef]
19. Smolenskii, G.I.V.; Agranovskaya, A.; Krainik, N. New ferroelectrics of complex composition IV. *Sov. Phys. Solid State* **1961**, *2*, 2651–2654.
20. Aksel, E.; Jones, J.L. Advances in lead-free piezoelectric materials for sensors and actuators. *Sensors* **2010**, *10*, 1935–1954. [CrossRef]
21. Miriyala, K.; Ramadurai, R. Microstructural influence on ferroelectric domain pattern and piezoelectric properties of $Na_{0.5}Bi_{0.5}TiO_3$ thin films. *Ceram. Int.* **2018**, *44*, 14556–14562. [CrossRef]
22. Scarisoreanu, N.; Craciun, F.; Ion, V.; Birjega, S.; Dinescu, M. Structural and electrical characterization of lead-free ferroelectric $Na_{1/2}Bi_{1/2}TiO_3$–$BaTiO_3$ thin films obtained by PLD and RF-PLD. *Appl. Surf. Sci.* **2007**, *254*, 1292–1297. [CrossRef]
23. Zhou, Z.H.; Xue, J.M.; Li, W.Z.; Wang, J.; Zhu, H.; Miao, J.M. Ferroelectric and electrical behavior of $(Na_{0.5}Bi_{0.5})TiO_3$ thin films. *Appl. Phys. Lett.* **2004**, *85*, 804–806. [CrossRef]
24. Quignon, S.; Soyer, C.; Rémiens, D. Synthesis and electrical properties of sputtered $(Na_{0.5}Bi_{0.5})TiO_3$ thin films on silicon substrate. *J. Am. Ceram. Soc.* **2012**, *95*, 3180–3184. [CrossRef]
25. Wu, J.; Wang, J. Multiferroic behaviour and orientation dependence of lead-free $(1-x)BiFeO_3$–$x(Bi_{0.50}Na_{0.50})TiO_3$ thin films. *J. Phys. D Appl. Phys.* **2009**, *42*, 195405. [CrossRef]
26. Rémondière, F.; Wu, A.; Vilarinho, P.M.; Mercurio, J.P. Piezoforce microscopy study of lead-free perovskite $Na_{0.5}Bi_{0.5}TiO_3$ thin films. *Appl. Phys. Lett.* **2007**, *90*, 152905. [CrossRef]

27. Yu, T.; Kwok, K.; Chan, H. Preparation and properties of sol–gel-derived $Bi_{0.5}Na_{0.5}TiO_3$ lead-free ferroelectric thin film. *Thin Solid Films* **2007**, *515*, 3563–3566. [CrossRef]

28. Daryapurkar, A.; Kolte, J.; Apte, P.; Gopalan, P. Structural and electrical properties of sodium bismuth titanate ($Na_{0.5}Bi_{0.5}TiO_3$) thin films optimized using the Taguchi approach. *Ceram. Int.* **2014**, *40*, 2441–2450. [CrossRef]

29. Scarisoreanu, N.D.; Craciun, F.; Chis, A.; Birjega, R.; Moldovan, A.; Galassi, C.; Dinescu, M. Lead-free ferroelectric thin films obtained by pulsed laser deposition. *Appl. Phys. A* **2010**, *101*, 747–751. [CrossRef]

30. Gallegos-Melgar, A.; Espinosa-Arbelaez, D.G.; Flores-Ruiz, F.J.; Lahmar, A.; Dellis, J.-L.; Lemee, N.; Espinoza-Beltran, F.J.; Saldana, J.M. Ferroelectric properties of manganese doped ($Bi_{1/2}Na_{1/2}$)TiO_3 and ($Bi1/2Na_{1/2}$)TiO_3-$BaTiO_3$ epitaxial thin films. *Appl. Surf. Sci.* **2015**, *359*, 923–930. [CrossRef]

31. Daryapurkar, A.; Kolte, J.; Gopalan, P. Influence of oxygen gas pressure on phase, microstructure and electrical properties of sodium bismuth titanate thin films grown using pulsed laser deposition. *Thin Solid Films* **2015**, *579*, 44–49. [CrossRef]

32. Hiruma, Y.; Imai, Y.; Watanabe, Y.; Nagata, H.; Takenaka, T. Large electrostrain near the phase transition temperature of ($Bi_{0.5}Na_{0.5}$)TiO_3–$SrTiO_3$ ferroelectric ceramics. *Appl. Phys. Lett.* **2008**, *92*, 262904. [CrossRef]

33. Hiruma, Y.; Nagata, H.; Takenaka, T. Phase diagrams and electrical properties of ($Bi_{1/2}Na_{1/2}$)TiO_3-based solid solutions. *J. Appl. Phys.* **2008**, *104*, 124106. [CrossRef]

34. Tadashi, T.; Kei-ichi, M.; Koichiro, S. ($Bi_{1/2}Na_{1/2}$)TiO_3-$BaTiO_3$ system for lead-free piezoelectric ceramics. *Jap. J. Appl. Phys.* **1991**, *30*, 2236.

35. Cao, W.; Li, W.; Xu, D.; Hou, Y.; Wang, W.; Fei, W. Enhanced electrocaloric effect in lead-free NBT-based ceramics. *Ceram. Int.* **2014**, *40*, 9273–9278. [CrossRef]

36. Cao, W.; Li, W.; Dai, X.; Zhang, T.; Sheng, J.; Hou, Y.; Fei, W. Large electrocaloric response and high energy-storage properties over a broad temperature range in lead-free NBT-ST ceramics. *J. Eur. Ceram. Soc.* **2016**, *36*, 593–600. [CrossRef]

37. Tang, J.; Wang, F.; Zhao, X.; Luo, H.; Luo, L.; Shi, W. Influence of the composition-induced structure evolution on the electrocaloric effect in $Bi_{0.5}Na_{0.5}TiO_3$-based solid solution. *Ceram. Int.* **2015**, *41*, 5888–5893. [CrossRef]

38. Hundt, C. Bleifreie Perowskite für die Elektrokalorik: Bismut-Natrium-Titanat. Master's Thesis, Technical University Dresden, Dresden, Germany, 2019.

39. Andrei, A.C.; Scarisoreanu, N.D.; Birjega, R.; Dinescu, M.; Stanciu, G.; Craciun, F.; Galassi, C. Pulsed laser deposition of lead-free ($Na_{0.5}Bi_{0.5}$)$_{1−x}Ba_xTiO3$ ferroelectric thin films with enhanced dielectric properties. *Appl. Surf. Sci.* **2013**, *278*, 162–165. [CrossRef]

40. Scott, J.F. Ferroelectrics go bananas. *J. Phys. Condens. Matter* **2007**, *20*, 021001. [CrossRef]

41. Schenk, T.; Yurchuk, E.F.; Mueller, S.M.; Schroeder, U.; Starschich, S.; Bottger, U.; Mikolajick, T. About the deformation of ferroelectric hystereses. *Appl. Phys. Rev.* **2014**, *1*, 041103. [CrossRef]

42. Liu, G.; Zhang, S.; Jiang, W.; Cao, W. Losses in ferroelectric materials. *Mater. Sci. Eng. R Rep.* **2015**, *89*, 1–48. [CrossRef] [PubMed]

43. Bousquet, M.; Duclère, J.-R.; Gautier, B.; Boulle, A.; Wu, A.; Deputier, S.; Fasquelle, D.; Rémondière, F.; Albertini, D.; Champeaux, C.; et al. Electrical properties of (110) epitaxial lead-free ferroelectric $Na_{0.5}Bi_{0.5}TiO_3$ thin films grown by pulsed laser deposition: Macroscopic and nanoscale data. *J. Appl. Phys.* **2012**, *111*, 104106. [CrossRef]